arXiv:2110.11058v4 [cond-mat.mes-hall] 9 Jun 2022

Unprotected quadratic band crossing points and quantum anomalous Hall effect in FeB_2 monolayer

Dongyu Wu,[1,2,*] Yunpeng Huang,[1,*] Song Sun,[1,2] Jiacheng Gao,[1,2] Zhaopeng Guo,[1,†] Hongming Weng,[1,2] Zhong Fang,[1,2] Kun Jiang,[1] and Zhijun Wang[1,2,‡]

[1] *Beijing National Laboratory for Condensed Matter Physics, and Institute of Physics, Chinese Academy of Sciences, Beijing 100190, China*
[2] *University of Chinese Academy of Sciences, Beijing 100049, China*

(Dated: June 10, 2022)

Quadratic band crossing points (QBCPs) and quantum anomalous Hall effect (QAHE) have attracted the attention of both theoretical and experimental researchers in recent years. Based on first-principle calculations, we find that the FeB_2 monolayer is a nonmagnetic semimetal with QBCPs at K. Through symmetry analysis and $\mathbf{k}\cdot\mathbf{p}$ invariant theory, we find that the QBCP is not protected by rotation symmetry and consists of two Dirac points with same chirality (Berry phase of 2π). Once introducing Coulomb interactions, we find that there is a spontaneous-time-reversal-breaking instability of the spinful QBCPs, which gives rise to a $C = 2$ QAH insulator with orbital moment ordering.

I. INTRODUCTION

In a two-dimensional (2D) system, the finite density of states associated with the parabolic dispersion could lead to instability for arbitrarily weak interactions [1–5]. For a quadratic band crossing point (QBCP) being stable without fine-tuning, the system must be time-reversal invariant and the QBCP must have C_4 or C_6 rotational symmetry [1]. An interaction would lead to the possibility of spontaneous breaking of rotational symmetry (nematic phase) or time-reversal invariance. However, the QBCPs at the threefold-invariant momentum on the honeycomb lattice and relatives are unprotected. The introduction of interactions leads to qualitatively different low-energy behavior without breaking the underlying symmetries [2]. Although there are many theoretical studies of spinless QBCPs on many tailored 2D systems, such as single-layer graphene [2, 3] and Bernal-stacked bilayer graphene [4], the unprotected QBCPs have not been reported in any spinful system and their possible instabilities have not been discussed yet.

Besides, topological states, including quantum anomalous Hall (QAH) state, have attracted considerable research interest recently [6–13]. In spite of plenty of material proposals for QAH state [14–19], the observation of the QAH effect is still full of challenges and has been merely realized in a few systems such as, Cr-doped and V-doped $(Bi,Sb)_2Te_3$ thin films [20, 21], magnetic topological insulator $MnBi_2Te_4$ [22] and twisted bilayer graphene (TBG) [23]. Previous theoretical studies also show that the QAH effect can be realized in graphene by introducing both exchange field and Rashba spin-orbit coupling (SOC) due to its unique linear Dirac band dispersions [15].

In recent years, MB_2 (M = transition metal) monolayers have been predicted to be 2D Dirac cone materials theoretically in the absence of SOC, such as TiB_2 [24], FeB_2 [25] and HfB_2 [26] monolayers. The FeB_2 bulk crystal has been grown [27]. The stability of the FeB_2 monolayer is predicted theoretically by structure searching, phonon spectra, and molecular dynamics [25, 28, 29]. Unlike graphene, the Dirac bands of FeB_2 originate from d states of the transition metal Fe, which has a substantial Rashba SOC effect and is very likely coupled to a magnetic field. A Chern insulator can be achieved once it is grown on an insulating magnetic substrate. In this article, we find that the FeB_2 monolayer is a nonmagnetic semimetal with QBCPs based on first-principle calculations. Without including SOC, there is a linearly dispersive Dirac node at K (resp. K') with a Berry phase π (resp. $-\pi$), protected by the combined symmetry of time reversal and twofold rotation (*i.e.*, TC_{2z}). Once including SOC, the Dirac node becomes a QBCP and its Berry phase becomes 2π (-2π) at K (K'). These characters can be captured by the $\mathbf{k}\cdot\mathbf{p}$ effective Hamiltonians. With an insulating magnetic substrate, the FeB_2 monolayer is turned to be a Chern insulator with two chiral edge states, which is stimulated by the fixed-moment calculations. More interestingly, once we introduce the Coulomb interactions, an instability towards a $C = 2$ QAH state with orbital moment ordering is found.

II. CALCULATION METHOD

We performed the first-principles calculations within the framework of the density functional theory (DFT) using the projector augmented wave (PAW) method [30, 31], which is implemented in Vienna *ab initio* simulation package (VASP) [32, 33]. The Perdew-Burke-Ernzerhof (PBE) generalized gradient approximation exchange-correlation functional [34] was implemented in calculations. The cut-off energy for plane wave expansion was

* These authors contributed equally to this work.
† zpguo@iphy.ac.cn
‡ wzj@iphy.ac.cn

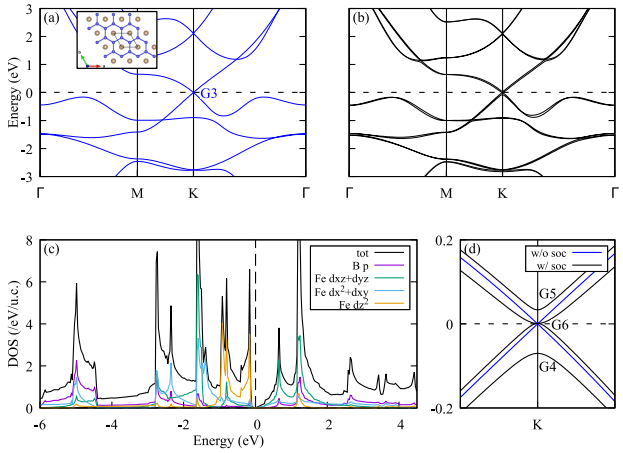


FIG. 1. (color online). The calculated electronic structures of FeB_2 monolayer without (a) and with (b) SOC. The inset in (a) shows the crystal structure of the FeB_2 monolayer, where Fe and B atoms are marked by brown and blue balls. The irrep of two-fold bands at K is denoted by G_3. (c) The total DOS and projected DOS of B-p and Fe-d orbitals, respectively. (d) The zoom-in plot of band structures near K point. The irreps of four low-energy SOC bands at K are denoted by G_4, G_5, and G_6.

945 eV, and $12 \times 12 \times 1$ k-point sampling grids were used in the self-consistent process. A vacuum layer of 20 Å was chosen to avoid interaction between neighboring layers. SOC was taken into account within the second variational method self-consistently. The irreducible representations (irreps) were obtained by the program IRVSP [36]. The maximally localized Wannier functions (MLWFs) were constructed by Fe-3d, B-2s and B-2p orbitals using Wannier90 package [37]. The edge states were calculated using surface Green's function of the semi-infinite system based on the iterative scheme [38–40].

III. DFT RESULTS

The crystal structure of FeB_2 monolayer belongs to space group $P6mm$ (No. 183), as shown in Fig. 1(a). One unit cell (a = 3.171 Å) contains two B atoms and one Fe atom, which are located at $2b$ and $1a$ Wyckoff positions, respectively. B atoms are arranged in a honeycomb lattice, and Fe atoms are located in the middle of the hexagons. The distance of Fe atoms and B atoms plane is 0.628 Å. The PBE band structure of FeB_2 monolayer is shown in Fig. 1(a), there is a linearly dispersive Dirac point at K near the Fermi level (E_F). Therefore, FeB_2 monolayer was predicted to be a 2D Dirac semimetal [25, 41]. The little point group at K is C_{3v}, and the twofold Dirac bands belong to G_3 irreducible representation (irrep), which is consistent with Ref. [41]. The total and projected density of states (DOS) are plotted in Fig. 1(c). They show that the hybridization between Fe and B is strong, while the electronic states

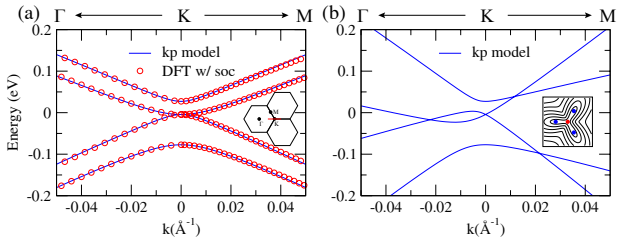


FIG. 2. (color online). (a) The band dispersions (blue lines) of the four-band effective Hamiltonian in Eq. (2) with the parameters in Table I agree well with the bands (red circles) from the DFT calculation. The k-path is indicated by the red line in the inset of the Brillouin zone. (b) The band dispersions of the effective model with $C_1 = -3.03$ eVÅ and $C_2 = -3.03$ eVÅ^2 are plotted for comparison. The inset shows iso-energy-gap lines in the vicinity of K point. The Dirac points with Berry phase π and $-\pi$ are colored in blue and red, respectively.

near E_F are mainly contributed by d_{z^2} and $d_{xz} + d_{yz}$ electrons of Fe atoms (the orbital-resolved band structures are given in Appendix A). Once including SOC, as shown in Figs. 1(b,d), the two Dirac bands split into two non-degenerate bands (G_4 and G_5) and one doubly-degenerate band (G_6) at K, exhibiting quadratic band dispersion.

IV. LOW-ENERGY EFFECTIVE MODELS

Based on the theory of invariants, we derive the low-energy effective Hamiltonian $H_K(\vec{k})$ (*i.e.*, $\vec{k}$ is the offset momentum from K). Under the basis of G_3 irrep, *e.g.* $\{|d_{xz} + id_{yz}\rangle, |d_{xz} - id_{yz}\rangle\}$, it reads,

$$H_K(\vec{k}) = \begin{pmatrix} M_1(\vec{k}) & Ak_+ \\ Ak_- & M_1(\vec{k}) \end{pmatrix}. \tag{1}$$

After considering the spin degree of freedom, the four-band Hamiltonian becomes (in the basis of $\{|\uparrow\rangle, |\downarrow\rangle\} \otimes \{|d_{xz} + id_{yz}\rangle, |d_{xz} - id_{yz}\rangle\}$),

$$H_K^{so}(\vec{k}) = \sigma_0 \otimes H_K(\vec{k}) + \begin{pmatrix} M_2(\vec{k}) & & & \dagger \\ 0 & -M_2(\vec{k}) & & \\ iBk_+ & iC(\vec{k}) & -M_2(\vec{k}) & \\ iM_3(\vec{k}) & iBk_+ & 0 & M_2(\vec{k}) \end{pmatrix}, \tag{2}$$

where $k_\pm = k_x \pm ik_y$, $C(\vec{k}) = C_1 k_- + C_2 k_+^2$, $M_{\alpha=1,2,3}(\vec{k}) = E_\alpha + F_\alpha k_\perp^2$ with $k_\perp^2 = k_x^2 + k_y^2$, and σ_0 is the identify matrix in spin space. Since the second-order k terms are crucial for the quadratic band dispersion in the following two-band model (which were omitted in Ref. [41]), we have derived them in the four-band $\mathbf{k}\cdot\mathbf{p}$ model as well.

By fitting the DFT band structure in the vicinity of K, the parameters are obtained in Table I and the results are shown in Fig. 2(a). The $\mathbf{k}\cdot\mathbf{p}$ model reproduces the QBCP at K, and the Berry phase for the QBCP is 2π. The $2nd$ and $3rd$ bases form G_6 irrep of C_{3v} double group, *i.e.*, $\{|d_{xz}-id_{yz},\uparrow\rangle, |d_{xz}+id_{yz},\downarrow\rangle\}$. To evaluate the positions of Dirac points, a simple model under G_6 irrep can be obtained as below,

$$H'_K(\vec{k}) = \begin{pmatrix} M_1(\vec{k}) - M_2(\vec{k}) & -iC_1k_+ - iC'_2k_-^2 \\ iC_1k_- + iC'_2k_+^2 & M_1(\vec{k}) - M_2(\vec{k}) \end{pmatrix}, \quad (3)$$

where C'_2 is a modified parameter after downfolding. Its two eigenvalues are solved as $E_\pm = M_1(\vec{k}) - M_2(\vec{k}) \pm \sqrt{\Delta(\vec{k})}$ with

$$\Delta(\vec{k}) = {C'_2}^2k_\perp^4 + 2C_1C'_2k_x(k_x^2 - 3k_y^2) + {C_1}^2k_\perp^2. \quad (4)$$

The gapless points satisfy the condition of $\Delta(\vec{k}) = 0$. Assuming $k_y = 0$, the equation is simplified to ${C'_2}^2k_x^4 + 2C_1C'_2k_x^3 + {C_1}^2k_x^2 = 0$, giving rise to two Dirac points located at $k_x = 0, -C_1/C'_2$. The detailed calculations show that the two Dirac points have opposite π Berry phase. The distance between them is $d_0 = |C_1/C'_2|$ in momentum space. Considering C_{3z} symmetry, there must be two additional Dirac points around K, as shown in the inset of Fig. 2(b). No other gapless point is found (see the proof in Appendix B).

As the Dirac points and the quantized Berry phase of π are protected by the antiunitary symmetry TC_{2z}, the above discussion should be valid for the four-band model $H_K^{so}(\vec{k})$ as well. In the band dispersions of Fig. 2(a), we numerically get $d_0 \sim 5.2\times10^{-5}$ Å^{-1}. The ration $d_0/d_{\Gamma K}$ is 0.004% ($d_{\Gamma K} = 1.321$ Å^{-1}), which is too small to identify in FeB_2 monolayer. Therefore, it's rational to consider the K point is a double Dirac point with quadratic band dispersions in FeB_2 monolayer, corresponding to a 2π Berry phase. As the quadratic band dispersion is not protected by rotational symmetry, it was previously considered as linear dispersion improperly [41]. Note that it's similar to the case in the magic-angle TBG, where the velocity of K becomes zero [42, 43]. For comparison, we plot the band dispersions of the four-band model with different C_1 and C_2 parameters in Fig. 2(b), from which d_0 is read to be 0.223 Å^{-1} ($\sim 0.17d_{\Gamma K}$). The iso-energy-gap contours are shown in the vicinity of K points in its inset. A Dirac point ($-\pi$) at K and three other Dirac points (π) are clearly shown.

TABLE I. The parameters in the effective $\mathbf{k}\cdot\mathbf{p}$ Hamiltonian.

0th order	eV	1st order	eV·Å	2nd order	eV·Å^2
E_1	-0.0147	A	2.6021	F_1	-1.7201
E_2	-0.0103	B	0.0141	F_2	0.2346
E_3	0.0522	C_1	-0.0080	F_3	0.5754
				C_2	-0.1010

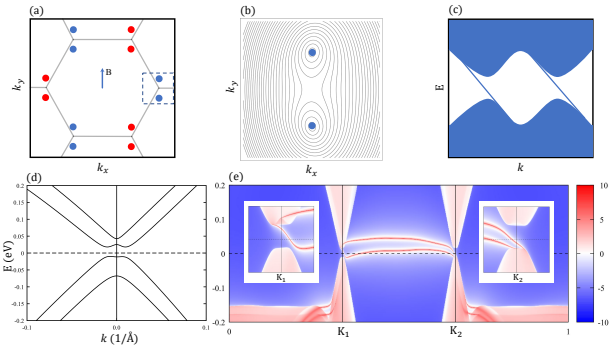


FIG. 3. (color online). The electronic structure of FeB_2 monolayer in a magnetic field. (a) The distribution of Dirac points with the in-plane magnetic field (which keeps TC_{2z}). The arrow marks the direction of the magnetic field. Each QBCP splits into two Dirac points with identical π Berry phase. (b) The iso-energy-gap contours are plotted in the dashed rectangle area in (a). (c) The schematic diagram of two chiral edge states of FeB_2 monolayer with z-directed magnetic field. (d) The computed band structure of FeB_2 monolayer with a fixed magnetic moment 0.01 μ_B on each Fe atom. (e) The B-terminated zigzag-edge state of fixed magnetic moment FeB_2 monolayer. The inserts show the zoom-in plots around $K_{1,2}$. The K_1 and K_2 are the projections of K and K' on the edge.

With an external magnetic field, a Chern insulator can be achieved in FeB_2 monolayer (*e.g.*, grown on an insulating magnetic substrate). As shown in Figs. 3(a,b), with an in-plane external magnetic field (keeping TC_{2z}), the double Dirac point at K splits into two Dirac points with the same chirality. The positions of Dirac nodes with different strength and directions of the in-plane magnetic field are shown in Fig.S2. When the magnetism is out-of-plane, the FeB_2 becomes a Chern insulator with two chiral edge states in Fig. 3(c). The Zeeman's coupling Hamiltonian is given in Appendix C. To simulate the spin-polarized state of FeB_2 induced by the out-of-plane magnetism of substrates, we have performed the DFT calculations with a fixed moment (*e.g.* 0.01 μ_B on each Fe atom) in z direction. Its spin-polarized band structure is obtained in Fig. 3(d). The FeB_2 monolayer becomes a Chern insulator, which is compatible with the result of graphene with both Rashba SOC and an exchange field [15]. Then, we construct the maximally localized Wannier functions (MLWFs) and calculate the edge spectra, as shown in Fig. 3(e). Two chiral edge states connecting the conduction continuum and valence continuum indicate a Chern number of 2.

V. ORBITAL-MOMENT-INDUCED QAHE WITH INTERACTIONS

Interestingly, once considering onsite Coulomb interaction, we find the instability towards a gapped phase with orbital moment ordering, and the system exhibiting a QAH effect. Using d_{xz}, d_{yz} and d_{z^2} orbitals of Fe

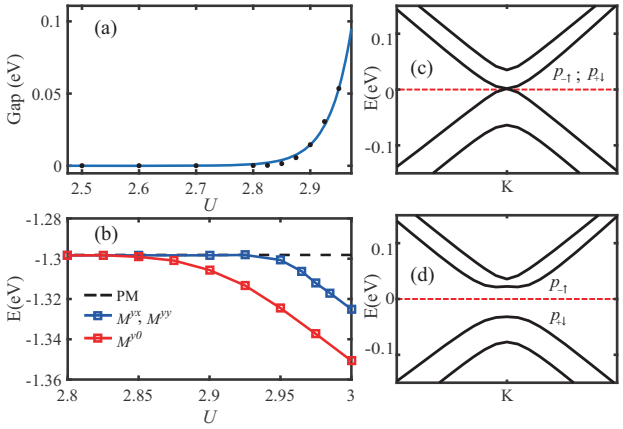


FIG. 4. (a) The energy gap behavior of the M^{y0} phase when varying the Coulomb interaction strength U, the solid blue line is fitting to the data by exponential function $\Delta = a * \exp(-1/(b * U))$ with $a = 3.812 \times 10^{30}$ and $b = 4.622 \times 10^{-3}$. (b) The energy of the obtained states in the self-consistency calculation as a function of the interaction strength U. (c-d) The quasiparticle energy bands when $U = 0$ and $U = 2.95\,eV$, the orbital characters of QBCP are also shown. The basis $P_{\pm\alpha} = \frac{1}{\sqrt{2}}(d_{xz,\alpha} \pm i d_{yz,\alpha})$, $\alpha = \uparrow, \downarrow$ We fixed $U = U'$ in the calculation of all figures.

atoms, a spinful three-orbital tight-binding model is constructed to capture the DFT band structure (see more details in Appendix D). The Coulomb interaction considered in d_{xz} and d_{yz} orbitals is written as,

$$H_{int} = U\sum_{l} n_{l,\uparrow}n_{l,\downarrow} + U'\sum_{l<l',\alpha\beta} n_{l,\alpha}n_{l',\beta}, \qquad (5)$$

where $n_{l,\alpha}$ represents the electron density on orbital l with spin α and $\alpha, \beta = \uparrow, \downarrow$. We further employ the Hartree-Fock approximation to treat the Coulomb interaction (The results of the LDA+U method are discussed in Appendix E). And the order parameters are defined as

$$M^{\mu\nu} = \sum_{l,l'}\sum_{\alpha,\beta} \tau^{\mu}_{l,l'}\sigma^{\nu}_{\alpha,\beta}\langle d^{\dagger}_{l,\alpha} d_{l',\beta}\rangle. \qquad (6)$$

Here, the $d^{(\dagger)}_{l,\alpha}$ operator annihilates (creates) an electron in orbital l and spin α. τ^{μ} and σ^{ν} $(\mu, \nu = 0, x, y, z)$ are the identity with three Pauli matrices representing the orbital and spin degree of freedom respectively. We self-consistently investigate the zero-temperature phase diagram, and the results are shown in Fig. 4.

In self-consistent calculations, we exclude the channels for SOC relevant order parameter M^{yz} and the symmetric part of the electron density terms M^{00}, which are already considered in the DFT calculation. After considering all other order parameters, we find that the Coulomb interaction between d_{xz} and d_{yz} orbitals intrinsically stimulates orbital-magnetization phases respectively with order parameters M^{yx}, M^{yy} and M^{y0}. These three orderings break the $TC_{2z} = i\tau_z \otimes \sigma_x\mathcal{K}$ symmetry and open the gap at the K point. The M^{yx} phase and M^{yy} phase are related by C_{6z} symmetry with relative higher energy, while the M^{y0} phase with orbital moment ordering is the ground state. The gap width exponentially grows when increasing the Coulomb interaction strength U in Fig.4(a). The gapped system then becomes a $C = 2$ Chern insulator.

VI. CONCLUSION

In conclusion, we have explored electronic structures and the topological property of the FeB_2 monolayer. Without SOC, the FeB_2 monolayer has linear band crossing points at K points. Upon including SOC, they become QBCPs with Berry phase 2π. Based on effective Hamiltonians, we demonstrate that the QBCPs are not protected by rotational symmetry. The appearance of QBCPs (or zero velocity at K) is similar to the case in the magic-angle TBG. FeB_2 monolayer is a good platform for studying the instability of spinful QBCPs. Considering Coulomb interaction in the spinful model of FeB_2 with QBCPs, it turns out to be a $C = 2$ QAH insulator with orbital moment ordering.

ACKNOWLEDGMENTS

This work was supported by the National Natural Science Foundation of China (Grants No. 11974395, 12188101, U2032204), the Strategic Priority Research Program of Chinese Academy of Sciences (Grant No. XDB33000000), China Postdoctoral Science Foundation funded project (Grant No. 2021M703461), and the Center for Materials Genome.

[1] K. Sun, H. Yao, E. Fradkin, and S. A. Kivelson, Phys. Rev. Lett. **103**, 046811 (2009).
[2] S. Hesselmann, C. Honerkamp, S. Wessel, and T. C. Lang, Phys. Rev. B **101**, 075128 (2020).
[3] G. Montambaux, The European Physical Journal B **85**, 375 (2012).
[4] O. Vafek and K. Yang, Phys. Rev. B **81**, 041401 (2010).
[5] Q.-F. Liang, J. Zhou, R. Yu, X. Wang, and H. Weng, Phys. Rev. B **96**, 205412.
[6] B. A. Bernevig, T. L. Hughes, and S.-C. Zhang, Science **314**, 1757 (2006).

[7] H. Zhang, C.-X. Liu, X.-L. Qi, X. Dai, Z. Fang, and S.-C. Zhang, Nat. Phys. **5**, 438 (2009).
[8] S. Nie, L. Xing, R. Jin, W. Xie, Z. Wang, and F. B. Prinz, Phys. Rev. B **98**, 125143 (2018).
[9] X. Wan, A. M. Turner, A. Vishwanath, and S. Y. Savrasov, Phys. Rev. B **83**, 205101 (2011).
[10] H. Weng, C. Fang, Z. Fang, B. A. Bernevig, and X. Dai, Phys. Rev. X **5**, 011029 (2015).
[11] S.-Y. Xu, I. Belopolski, N. Alidoust, M. Neupane, G. Bian, C. Zhang, R. Sankar, G. Chang, Z. Yuan, C.-C. Lee, S.-M. Huang, H. Zheng, J. Ma, D. S. Sanchez, B. Wang, A. Bansil, F. Chou, P. P. Shibayev, H. Lin, S. Jia, and M. Z. Hasan, Science **349**, 613 (2015).
[12] Z. Wang, M. G. Vergniory, S. Kushwaha, M. Hirschberger, E. V. Chulkov, A. Ernst, N. P. Ong, R. J. Cava, and B. A. Bernevig, Phys. Rev. Lett. **117**, 236401 (2016).
[13] D. J. Thouless, M. Kohmoto, M. P. Nightingale, and M. Dennijs, Phys. Rev. Lett. **49**, 405 (1982).
[14] R. Yu, W. Zhang, H.-J. Zhang, S.-C. Zhang, X. Dai, and Z. Fang, Science **329**, 61 (2010).
[15] Z. Qiao, S. A. Yang, W. Feng, W.-K. Tse, J. Ding, Y. Yao, J. Wang, and Q. Niu, Phys. Rev. B **82**, 161414 (2010).
[16] K. F. Garrity and D. Vanderbilt, Phys. Rev. Lett. **110**, 116802 (2013).
[17] Y. Xue, J. Y. Zhang, B. Zhao, X. Y. Wei, and Z. Q. Yang, Nanoscale **10**, 8569 (2018).
[18] Z. F. Wang, Z. Liu, and F. Liu, Phys. Rev. Lett. **110**, 196801 (2013).
[19] S. Nie, Y. Sun, F. B. Prinz, Z. Wang, H. Weng, Z. Fang, and X. Dai, Phys. Rev. Lett. **124**, 076403 (2020).
[20] C.-Z. Chang, J. Zhang, X. Feng, J. Shen, Z. Zhang, M. Guo, K. Li, Y. Ou, P. Wei, L.-L. Wang, Z.-Q. Ji, Y. Feng, S. Ji, X. Chen, J. Jia, X. Dai, Z. Fang, S.-C. Zhang, K. He, Y. Wang, L. Lu, X.-C. Ma, and Q.-K. Xue, Science **340**, 167 (2013).
[21] C.-Z. Chang, W. Zhao, D. Y. Kim, H. Zhang, B. A. Assaf, D. Heiman, S.-C. Zhang, C. Liu, M. H. W. Chan, and J. S. Moodera, Nat. Mater. **14**, 473 (2015).
[22] Y. Deng, Y. Yu, M. Z. Shi, Z. Guo, Z. Xu, J. Wang, X. H. Chen, and Y. Zhang, Science **367**, 895 (2020).
[23] M. Serlin, C. L. Tschirhart, H. Polshyn, Y. Zhang, J. Zhu, K. Watanabe, T. Taniguchi, L. Balents, and A. F. Young, Science **367**, 900 (2020).
[24] L. Z. Zhang, Z. F. Wang, S. X. Du, H. J. Gao, and F. Liu, Phys. Rev. B **90**, 161402 (2014).
[25] H. Zhang, Y. Li, J. Hou, A. Du, and Z. Chen, Nano Lett. **16**, 6124 (2016).
[26] Z. Liu, P. Wang, Q. Cui, G. Yang, S. Jin, and K. Xiong, Rsc Advances **9**, 2740 (2019).
[27] L. Voroshin, L. Lyakhovich, G. Panich, and G. Protasevich, Met. Sci. Heat Treat. **12**, 732 (1970).
[28] X. Yang, Z. Dai, Y. Zhao, and S. Meng, Comp. Mater. Sci. **147**, 132 (2018).
[29] A. Ahmadi, M. Masoudi, N. Taghizade, H. Jafari, and M. Faghihnasiri, Phys. E Low-dimens. Syst. Nanostruct, **112**, 71 (2019).
[30] P. E. Blochl, Phys. Rev. B **50**, 17953 (1994).
[31] G. Kresse and D. Joubert, Phys. Rev. B **59**, 1758 (1999).
[32] G. Kresse and J. Furthmuller, Comp. Mater. Sci. **6**, 15 (1996).
[33] G. Kresse and J. Furthmuller, Phys. Rev. B **54**, 11169 (1996).
[34] J. P. Perdew, K. Burke, and M. Ernzerhof, Phys. Rev. Lett. **77**, 3865 (1996).
[35] S. L. Dudarev, G. A. Botton, S. Y. Savrasov, C. J. Humphreys, and A. P. Sutton, Phys. Rev. B **57**, 1505 (1998).
[36] J. C. Gao, Q. S. Wu, C. Persson, and Z. J. Wang, Comp. Phys. Commun. **261**, 107760 (2021).
[37] G. Pizzi, V. Vitale, R. Arita, S. Bluegel, F. Freimuth, G. Geranton, M. Gibertini, D. Gresch, C. Johnson, T. Koretsune, J. Ibanez-Azpiroz, H. Lee, J.-M. Lihm, D. Marchand, A. Marrazzo, Y. Mokrousov, J. I. Mustafa, Y. Nohara, Y. Nomura, L. Paulatto, S. Ponce, T. Ponweiser, J. Qiao, F. Thoele, S. S. Tsirkin, M. Wierzbowska, N. Marzari, D. Vanderbilt, I. Souza, A. A. Mostofi, and J. R. Yates, J. Phys.-Condens. Matter **32**, 165902 (2020).
[38] M. P. L. Sancho, J. M. L. Sancho, and J. Rubio, J. Phys. F-Met. Phys. **14**, 1205 (1984).
[39] M. P. L. Sancho, J. M. L. Sancho, and J. Rubio, J. Phys. F-Met. Phys. **15**, 851 (1985).
[40] Q. Wu, S. Zhang, H.-F. Song, M. Troyer, and A. A. Soluyanov, Comp. Phys. Commun. **224**, 405 (2018).
[41] W. Luo, J. Ji, J. Lu, X. Zhang, and H. Xiang, Phys. Rev. B **101**, 195111 (2020).
[42] R. Bistritzer and A. H. MacDonald, Proc. Natl. Acad. Sci. USA **108**, 12233 (2011).
[43] Z. Song, Z. Wang, W. Shi, G. Li, C. Fang, and B. A. Bernevig, Phys. Rev. Lett. **123**, 036401 (2019).

APPENDIX

A. Orbital-resolved band structures

The orbital-resolved band structures are presented in Fig. S1. We found that the low-energy bands near E_F (*i.e.*, $-3eV < E - E_F < 1eV$) mainly come from Fe-d orbitals.

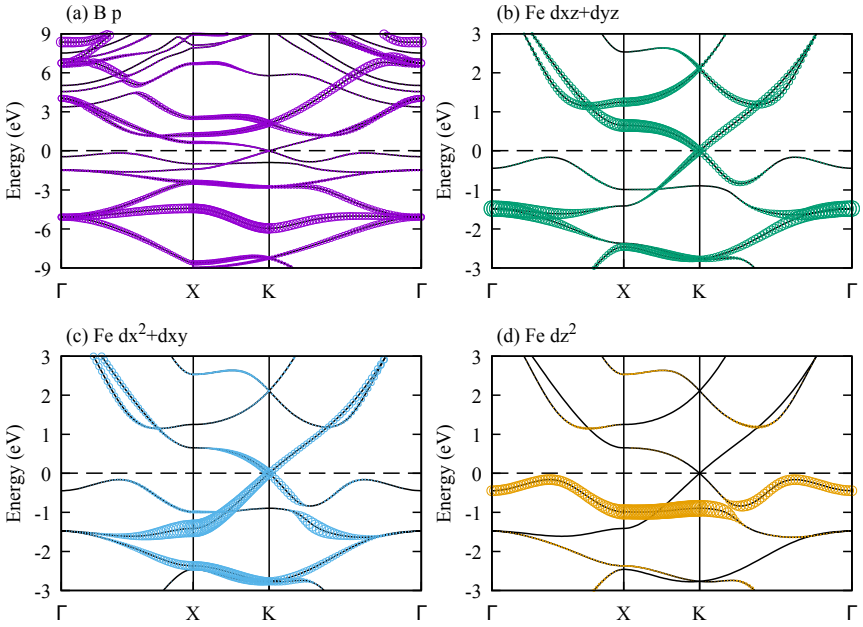


FIG. S1. (color online). The orbital-resolved band structures of monolayer FeB_2 of (a)p orbitals of B atoms, (b)$d_{xz} + d_{yz}$, (c)$d_{x^2-y^2} + d_{xy}$ and (d)d_{z^2} orbitals of Fe atom.

B. Low-energy effective Hamiltonians

Without SOC, the band crossing at K belongs to two-dimensional irreducible representation (irrep) G_3 (labeled in the double point group of C_{3v}). When considering SOC, it changes into $G_4 \oplus G_5 \oplus G_6$ irreps. We choose the bases of $\{|\uparrow\rangle, |\downarrow\rangle\} \otimes \{|d_{xz} + id_{yz}\rangle, |d_{xz} - id_{yz}\rangle\}$ to construct the 4×4 Hamiltonian. The $\mathbf{k} \cdot \mathbf{p}$ Hamiltonian around K is constrained by the double point group C_{3v} and an anti-unitary symmetry TC_{2z}. Under these bases, the generators (*e.g.* C_{3z}, M_y, and $C_{6z}T$) are represented as follows,

$$C_{3z} = \begin{pmatrix} -1 & 0 & 0 & 0 \\ 0 & e^{i\pi/3} & 0 & 0 \\ 0 & 0 & e^{-i\pi/3} & 0 \\ 0 & 0 & 0 & -1 \end{pmatrix}, \tag{7}$$

$$M_y = \begin{pmatrix} 0 & 0 & 0 & 1 \\ 0 & 0 & 1 & 0 \\ 0 & -1 & 0 & 0 \\ -1 & 0 & 0 & 0 \end{pmatrix}, \tag{8}$$

$$C_{6z}T = \begin{pmatrix} 0 & 0 & 0 & i \\ 0 & 0 & -e^{i\pi/6} & 0 \\ 0 & e^{-i\pi/6} & 0 & 0 \\ i & 0 & 0 & 0 \end{pmatrix} \mathcal{K}, \tag{9}$$

where $\mathcal{K}$ denotes the complex conjugation. Using the theory of invariants, we constructed the $\mathbf{k}\cdot\mathbf{p}$ effective Hamiltonian below,

$$H_K^{so}(\vec{k}) = \begin{pmatrix} M_1(\vec{k}) + M_2(\vec{k}) & & & \dagger \\ Ak_- & M_1(\vec{k}) - M_2(\vec{k}) & & \\ iBk_+ & iC(\vec{k}) & M_1(\vec{k}) - M_2(\vec{k}) & \\ iM_3(\vec{k}) & iBk_+ & Ak_- & M_1(\vec{k}) + M_2(\vec{k}) \end{pmatrix}, \tag{10}$$

where $k_\pm = k_x \pm ik_y$, $C(\vec{k}) = C_1k_- + C_2k_+^2$, and $M_{\alpha=1,2,3}(\vec{k}) = E_\alpha + F_\alpha k_\perp^2$ with $k_\perp^2 = k_x^2 + k_y^2$. On the other hand, the simplest two-band $\mathbf{k}\cdot\mathbf{p}$ Hamiltonian under the two bases of G_6 irrep is also derived as,

$$H'_K(\vec{k}) = \begin{pmatrix} M_1(\vec{k}) - M_2(\vec{k}) & -iC_1k_+ - iC_2'k_-^2 \\ iC_1k_- + iC_2'k_+^2 & M_1(\vec{k}) - M_2(\vec{k}) \end{pmatrix}. \tag{11}$$

Then, we will prove there are only four Dirac points in the above two-band Hamiltonian. With the condition $k_x = ak_y$ ($a \neq 0$), we will get solutions ($k_x = (a^2(3-a^2)C_1/C_2' \pm \sqrt{-(3a^3-a)^2(C_1/C_2')^2})/(1+a^2)^2, k_y = k_x/a$). To get real roots of the solutions, $\sqrt{-(3a^3-a)^2(C_1/C_2')^2}$ should be zero. If $C_1/C_2' \neq 0$ and $a \neq 0$, then $3a^2 - 1 = 0$, thus $a = \pm\sqrt{3}/3$. Taking $k_x = \pm k_y/\sqrt{3}$ into the equation, we can get the positions of two Dirac points, which are $(C_1/2C_2', \pm\sqrt{3}C_1/2C_2')$. Combining the results of conditions $k_x = 0$, $k_y = 0$ and $k_x = ak_y$ ($a \neq 0$), there are four Dirac points in two-band $\mathbf{k}\cdot\mathbf{p}$ Hamiltonian of G_6 irrep. One Dirac point is located at $(0,0)$, and three C_3-related Dirac points are located at $(-C_1/C_2', 0)$ and $(C_1/2C_2', \pm\sqrt{3}C_1/2C_2')$. These three Dirac points are connected by C_3 symmetry, and their distances from K are $d_0 = |C_1/C_2'|$. Thus, with the $|C_1/C_2'|$ decreases, the Dirac points will come close to the K point. If C_1 decrease to zero, the eigenvalues of Eq. (11) are $E_\pm = M_1(\vec{k}) - M_2(\vec{k}) \pm |C_2'|(k_x^2 + k_y^2) = E_1 - E_2 + (F_1 - F_2 \pm |C_2'|)k_\perp^2$, indicating a quadratic dispersion around K, corresponding to a double Dirac point with 2π Berry phase.

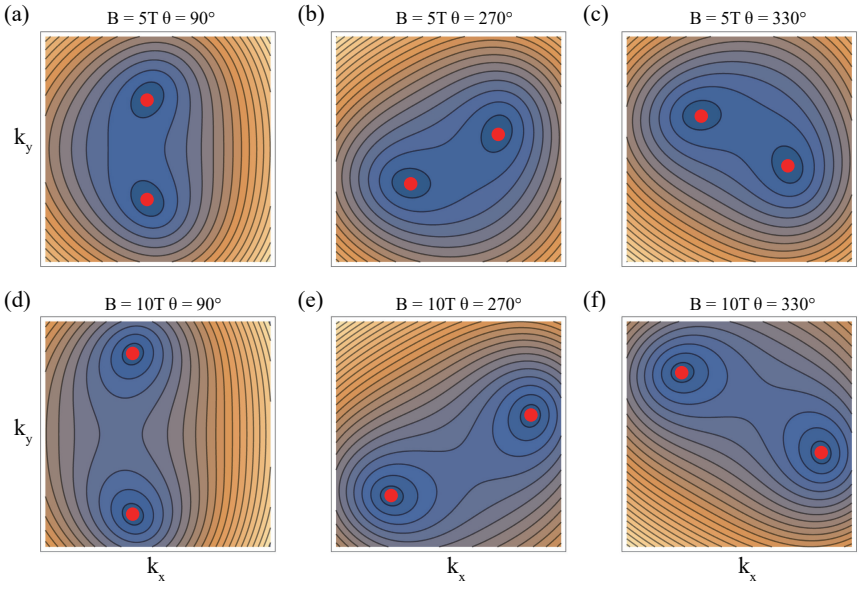


FIG. S2. (color online).The iso-energy-gap contours in rectangle area with 5×10^{-4} Å^{-1} around K under (a-c)5T and (d-f)10T with different directions of the in-plane magnetic field. The positions of Dirac nodes are marked by red dots. The angle between the magnetic field and the x axis located in the xy plane is marked by θ.

C. Zeeman splitting under magnetic field

The Zeeman's coupling is obtained as,

$$H^Z(\vec{B}) = \mu_B \begin{pmatrix} g_\parallel^{\frac{3}{2}} B_z & & & \dagger \\ ig'_\perp B_- & -g_\parallel^{\frac{1}{2}} B_z & & \\ g''_\perp B_+ & g_\perp^{\frac{1}{2}} B_- & g_\parallel^{\frac{1}{2}} B_z & \\ 0 & g''_\perp B_+ & ig'_\perp B_- & -g_\parallel^{\frac{3}{2}} B_z \end{pmatrix}, \tag{12}$$

where $B_\pm = B_x \pm iB_y$ and $\mu_B = \frac{e\hbar}{2m_e}$ is Bohr magneton. Under in-plane magnetic field (which keeps TC_{2z}), the double Dirac point splits into two Dirac points with identical Berry phase π, as shown in Fig. 3(a,b) and Fig. S2. Besides, we consider in-plane magnetic fields with different strengths and directions, and find that the Dirac nodes move away from K when increasing the magnetic field. Then we consider the external magnetic field in the z direction (breaking TC_{2z}). This Zeeman field will open an energy gap at both K points, giving rise to a Chern insulator with $C = 2$.

D. Three-orbital tight-binding model

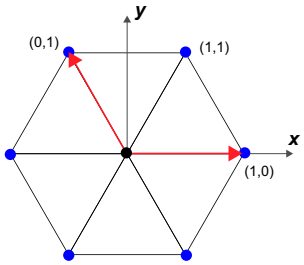


FIG. S3. The lattice of the tight-binding model with a lattice constant a. The 1a Wyckoff site is (0,0) with respect to the lattice vectors, denoted by two red-colored arrows.

To capture the Dirac points at K points, the elementary band representations have to be $\{A_1@1a$ and $E_1@1a\}$ in the absence of SOC. Thus we choose d_{xz}, d_{yz}, d_{z^2} orbitals of Fe atom to build the tight-binding model. The state $|d_\alpha, (00)\rangle$ defines the orbital d_α in the unit cell (mn) with respect to lattice rectors (lattice constant a), as shown in Fig. S3. Only the nearest neighbor hoppings are considered.

Consider the spin degree of freedom, the 6×6 tight-binding (tb) Hamiltonian is given below,

$$H_{tb} = \sigma_0 \otimes H(\vec{k}) + H_{so}(\vec{k}),\ H_{so}(\vec{k}) = \begin{pmatrix} \Lambda_0(\vec{k}) & \Lambda_1(\vec{k}) \\ -\Lambda_1^T(-\vec{k}) & \Lambda_0^T(-\vec{k}) \end{pmatrix} \tag{13}$$

The $H(\vec{k}), \Lambda_0(\vec{k}), \Lambda_1(\vec{k})$ are 3×3 matrices with $\vec{k}$ given in units of $1/a$. The up-triangle elements of the Hermitian

matrix $H(\vec{k})$ without SOC are given as follows,

$$
\begin{aligned}
H_{11}(\vec{k}) &= \epsilon_1 + 2t_1\cos k_x + (t_1+3t_2)\cos\frac{k_x}{2}\cos\frac{\sqrt{3}}{2}k_y \\
H_{22}(\vec{k}) &= \epsilon_1 + 2t_2\cos k_x + (3t_1+t_2)\cos\frac{k_x}{2}\cos\frac{\sqrt{3}}{2}k_y \\
H_{33}(\vec{k}) &= \epsilon_2 + 2t_3[\cos k_x + \cos(\frac{k_x}{2}+\frac{\sqrt{3}}{2}k_y) + \cos(-\frac{k_x}{2}+\frac{\sqrt{3}}{2}k_y)] \\
H_{12}(\vec{k}) &= \sqrt{3}(t_2-t_1)\sin\frac{k_x}{2}\sin\frac{\sqrt{3}}{2}k_y \\
H_{13}(\vec{k}) &= it_4[2\sin k_x + \sin(\frac{k_x}{2}+\frac{\sqrt{3}}{2}k_y) - \sin(-\frac{k_x}{2}+\frac{\sqrt{3}}{2}k_y)] \\
H_{23}(\vec{k}) &= i\sqrt{3}t_4[\sin(\frac{k_x}{2}+\frac{\sqrt{3}}{2}k_y) + \sin(-\frac{k_x}{2}+\frac{\sqrt{3}}{2}k_y)] \\
&\text{with } \epsilon_1 = \langle d_{xz},(00)|H|d_{xz},(00)\rangle, \epsilon_2 = \langle d_{z^2},(00)|H|d_{z^2},(00)\rangle, t_1 = \langle d_{xz},(00)|H|d_{xz},(10)\rangle, \\
&\quad t_2 = \langle d_{yz},(00)|H|d_{yz},(10)\rangle, t_3 = \langle d_{z^2},(00)|H|d_{z^2},(10)\rangle, t_4 = \langle d_{xz},(00)|H|d_{z^2},(10)\rangle.
\end{aligned}
\tag{14}
$$

The spin-orbit coupling terms of $\Lambda_0(\vec{k})$ and $\Lambda_1(\vec{k})$ are derived as,

$$
\begin{aligned}
\Lambda_0(\vec{k}) &= \begin{pmatrix} 0 & i\lambda_0 & 0 \\ -i\lambda_0 & 0 & 0 \\ 0 & 0 & 0 \end{pmatrix}, \ \Lambda_1(\vec{k}) = \begin{pmatrix} a(\vec{k}) & c(\vec{k}) & 0 \\ c(\vec{k}) & b(\vec{k}) & 0 \\ 0 & 0 & 0 \end{pmatrix}, \\
a(\vec{k}) &= 2i\lambda_1\sin k_x + 2ie^{-i\frac{\pi}{3}}(\frac{\lambda_1}{4}+\frac{3\lambda_2}{4})[\sin(\frac{k_x}{2}+\frac{\sqrt{3}k_y}{2}) + e^{-i\frac{\pi}{3}}\sin(-\frac{k_x}{2}+\frac{\sqrt{3}k_y}{2})] \\
b(\vec{k}) &= 2i\lambda_2\sin k_x + 2ie^{-i\frac{\pi}{3}}(\frac{3\lambda_1}{4}+\frac{\lambda_2}{4})[\sin(\frac{k_x}{2}+\frac{\sqrt{3}k_y}{2}) + e^{-i\frac{\pi}{3}}\sin(-\frac{k_x}{2}+\frac{\sqrt{3}k_y}{2})] \\
c(\vec{k}) &= i\frac{\sqrt{3}}{2}(\lambda_1-\lambda_2)[e^{-i\frac{\pi}{3}}\sin(\frac{k_x}{2}+\frac{\sqrt{3}k_y}{2}) + e^{i\frac{\pi}{3}}\sin(-\frac{k_x}{2}+\frac{\sqrt{3}k_y}{2})] \\
&\text{with } i\lambda_0 = \langle d_{xz\uparrow},(00)|H|d_{yz\uparrow},(00)\rangle, \\
&\quad \lambda_1 = \langle d_{xz\uparrow},(00)|H|d_{xz\downarrow},(10)\rangle, \lambda_2 = \langle d_{yz\uparrow},(00)|H|d_{yz\downarrow},(10)\rangle.
\end{aligned}
\tag{15}
$$

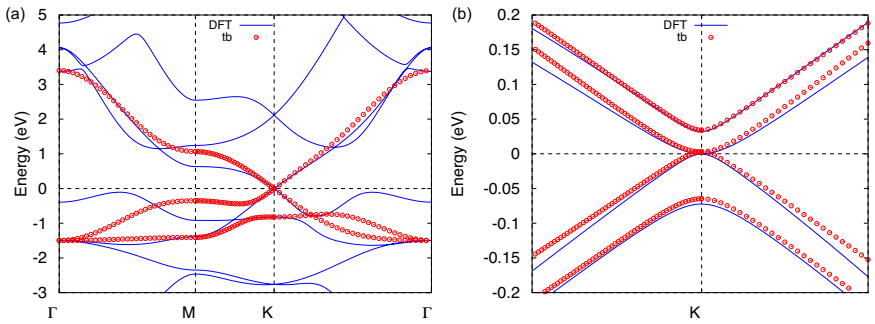


FIG. S4. The comparison between the DFT bands and the energy bands of the tight-binding model without (a) and with (b) SOC. The parameters are given in Table S1.

TABLE S1. The parameters in the tight-binding Hamiltonian are real and given in units of eV.

ϵ_1	ϵ_2	t_1	t_2	t_3	t_4	λ_1	λ_2	λ_0
-0.5036	0.5864	-0.475	0.1434	0.4689	-0.3500	-0.0290	-0.0100	0.008

By fitting the energy bands of the DFT calculation without SOC, the parameters of $\epsilon_1, \epsilon_2, t_1, t_2, t_3$ and t_4 are obtained. The three parameters $\lambda_{0,1,2}$ are obtained by fitting the DFT bands with SOC. These parameters are listed in Table S1, and the corresponding band structures are shown in Fig. S4.

E. The band structures of LDA+U method

We calculate the LDA+U and LDA+U+SOC band structures, and find that the quadratic band crossing points are preserved in LDA+U+SOC results, as shown in Fig.S5. We would like to emphasize here that the former LDA+U technic we used is based on Dudarev *et al.*'s work[35]. Only the density-related terms are counted in the approximation. However, the crucial inter-orbital correlation terms are not considered in these calculations. Thus, we think the normal LDA+U method is not a suitable method to explore the physics here.

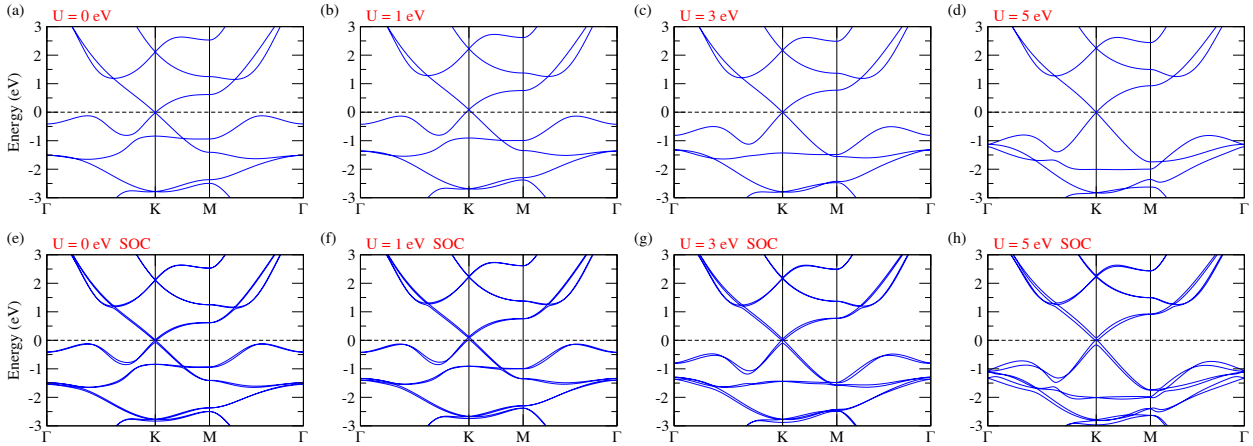


FIG. S5. (a-d)The band structures of FeB_2 monolayer with Hubbard U of 0, 1, 3, and 5 eV. (e-h)The LDA+U+SOC band structures of FeB_2 monolayer. The quadratic band crossing points are located at K.